


RESEARCH ARTICLE

Observations and high-resolution simulations of convective precipitation organization over the tropical Atlantic

Sebastian Brune  | Sebastian Buschow | Petra FriederichsInstitute of Geosciences, University of
Bonn, Germany**Correspondence**S. Brune, Institute of Geosciences,
University of Bonn, Auf dem Hügel 20,
53121 Bonn, Germany.
Email: sbrune@uni-bonn.de**Funding information**German Ministry for Education and
Research (BMBF) for the HD(CP)2,
FKZ01LK1507B**Abstract**

High-resolution simulations (grid spacing 2.5 km) are performed with ICON-LEM to characterize convective organization in the Tropics during August 2016 over a large domain ranging from northeastern South America, along the tropical Atlantic to Africa (8,000 × 3,000 km). The degree of organization is measured by a refined version of the wavelet-based organization index (WOI), which is able to characterize the scale, the intensity and anisotropy of convection based on rain rates alone. Exploiting the localization of wavelets both in space and time, we define a localized version of the convective organization index (LWOI). We compare convection observed in satellite-derived rain rates with the corresponding processes simulated by ICON-LEM. Model and observations indicate three regions with different kinds of convective organization. Continental convection over West Africa has a predominantly meridional orientation and is more organized than over South America, because it acts on larger scales and is more intense. Convection over the tropical Atlantic is zonally oriented along the ITCZ and less intense. ICON and observations agree on the number and intensity of the African easterly waves during the simulation period. The waves are associated with strong vorticity anomalies and are clearly visible in a spatiotemporal wavelet analysis. The central speed and the wavelength of the waves is simulated well. Both the scale and intensity components of LWOI in ICON are significantly correlated with environmental variables. The scale of precipitation is related to wind shear, CAPE and its tendency, while the intensity strongly correlates with column-integrated humidity, upper-level divergence and maximum vertical wind speed. This demonstrates that the LWOI components capture important characteristics of convective precipitation.

KEYWORDS

convective organization, ICON-LEM, IMERG, LWOI, tropical convection, wavelet-based organization index, WOI

This is an open access article under the terms of the Creative Commons Attribution License, which permits use, distribution and reproduction in any medium, provided the original work is properly cited.

© 2020 The Authors. *Quarterly Journal of the Royal Meteorological Society* published by John Wiley & Sons Ltd on behalf of the Royal Meteorological Society.

1 | INTRODUCTION

Convection and its organization play an essential role in the dynamics of the climate system. For instance, around 70% of the total global precipitation over land is caused by deep convection (Xu and Zipser, 2012). Besides moisture fluxes through condensation and rainfall, it has crucial influence on the energy and momentum transport in the global circulation (Stevens and Bony, 2013). Convective processes interact with the global circulation and are driven by large-scale forcing due to waves, fronts and convergence lines (Duda and Gallus Jr. 2013). Different forcing mechanisms and environmental quantities such as wind shear or instability lead to weakly (e.g. pulse storms, scattered convection) or strongly (e.g. squall-lines, mesoscale convective systems) organized convection. Phenomena in the latter category live on larger spatial and temporal scales and are linked to strong forcing and increased wind shear (Moncrieff, 2010). Supercells, squall-lines and other mesoscale convective systems (MCSs) are associated with e.g. large hail, severe winds, tornadoes and/or heavy rainfalls (Groenemeijer *et al.*, 2017). Thus, the correct representation of convection and its degree of organization in numerical weather and climate prediction systems is vitally important.

In recent years the resolution of numerical weather prediction models has increased rapidly (grid spacing \approx 1–10 km) and many convective processes are resolved explicitly. However, in climate simulations with general circulation models (grid spacing \approx 10–100 km), convection still needs to be parametrized to describe organized features like the Madden–Julian oscillation satisfactorily (Peters *et al.*, 2017). Convective parametrizations are responsible for large uncertainties in climate prediction models and are still under vital debate (e.g., Birch *et al.*, 2015; Badlan *et al.*, 2017; Holloway *et al.*, 2017; Moncrieff *et al.*, 2017; Wing *et al.*, 2017). One major aspect in current research is the question of whether and how convective organization should be parametrized (e.g., Mapes and Neale, 2011). Therefore different degrees of convective organization need to be quantified.

Especially in the Tropics, where convection acts on very different scales ranging from cumulus convection and pulse storms up to hurricanes or the Madden–Julian oscillation (Petersen and Rutledge, 2001), a correct representation of convective organization is important. Most tropical convection is driven by the intertropical convergence zone (ITCZ), but heterogeneous continental landmasses (e.g., Africa and South America) greatly influence its initiation and organization as well. Current general circulation models are not able to predict the exact position of the ITCZ correctly (Möbis and Stevens,

2012; Nolan *et al.*, 2016), with the consequence that convection and its degree of organization are represented inadequately.

In our study, we focus on the tropical Atlantic including the adjacent parts of South America and Africa in August 2016 to investigate convective processes over three different regions: the northeastern coast of South America including the Amazon and Tocantins delta, the tropical Atlantic along the ITCZ, and West Africa including western parts of Sahel, Guinea Highlands and Gulf of Guinea. Earlier studies have shown that the types of convection, its organization and the forcing mechanisms are fundamentally different within these regions. Garstang *et al.* (1994), Rickenbach (2004) and Romatschke and Houze Jr. (2010) have shown that convection over northeastern South America is initiated by convergence lines along the coastline due to the easterlies. Intense long-living MCSs (mostly squall-lines) develop, move inland and benefit from the relatively flat terrain and high moisture in the Amazon and Tocantins delta. Over Africa, convection is driven by the African easterly waves (AEWs). AEWs modulate organized convection over Africa (Duvel, 1990; Mekonnen and Rossow, 2018; Tomassini, 2018) and initiate strong squall-lines with heavy rainfall (e.g., Carlson, 1969; Fink and Reiner, 2003; Mekonnen *et al.*, 2006; Crétat *et al.*, 2015). AEWs, defined as westward propagating lower-tropospheric disturbances over Africa, have a period of 2.5–5 days (Burpee, 1972; Lubis and Jacobi, 2015) and a phase speed of 8–10 m·s⁻¹ (Reed *et al.*, 1977; Price *et al.*, 2007). The wavelength of AEWs ranges from 2,000 km (e.g., Burpee, 1974) up to 5,000 km (Diedhiou *et al.*, 1999; Kiladis *et al.*, 2006), which correspond to zonal wavenumbers between 8 and 19. Thus, strongly organized MCSs, frequently organized into squall-lines (Mathon and Laurent, 2001; Jackson *et al.*, 2009; Rickenbach *et al.*, 2009), move westward across the tropical Atlantic. The large-scale forcing over the tropical Atlantic is weaker than over Africa (Xie and Carton, 2004). In general there are fundamental differences between convection over land and ocean (Zipser *et al.*, 2006; Janiga and Thorncroft, 2013). Convection over the tropical Atlantic shows lower cloud tops and less intense rain rates, but more stratiform rainfall than over Africa (Schumacher and Houze Jr. 2006; Futyán and Del Genio, 2007; Liu *et al.*, 2007; Janiga and Thorncroft, 2014; 2016).

To characterize these regions of different convective organization, we use high-resolution convection-permitting simulations and compare them to two kinds of satellite-derived rain rate estimations, namely passive microwave radiometers and infrared measurements.

Senf *et al.* (2018), using the same dataset as the present study, evaluated brightness temperatures simulated by

the ICOSahedral Non-hydrostatic model (ICON) against satellite observations over the tropical Atlantic using a histogram matching technique. Their object-based analysis shows that ICON simulates convection more realistically over continental regions than over the ocean, but contains more small-scale features and overestimates shallow cumulus clouds.

Convective organization is generally measured by indices such as the simple convective aggregation index (SCAI; Tobin *et al.*, 2012), the organization index (I_{org} ; Tompkins and Semie, 2017) or the convective organization potential (COP; White *et al.*, 2018). These conventional indices are based on cluster algorithms of brightness temperatures, vertical wind velocity and outgoing long-wave radiation, respectively. A comparison of the different convective organization indices is presented in Pscheidt *et al.* (2019).

Local convective organization has previously been investigated by Li *et al.* (2018) calculating the information entropy (Shannon, 1948) from satellite observations. They find that information entropy shows only small variances between weak and strong convective organization. Thus, defining convective organization locally is still challenging.

In meteorology, wavelets are used to verify precipitation or cloud fields (e.g., Casati *et al.*, 2004; Yano and Jakubiak, 2016; Weniger *et al.*, 2017; Kapp *et al.*, 2018; Buschow *et al.*, 2019) or to characterize the structure of convection (e.g., Yano *et al.*, 2001a; Yano *et al.*, 2001b; Klein *et al.*, 2018). Brune *et al.* (2018) developed the wavelet-based organization index (WOI) to differentiate between non-organized and organized convection over Germany based on rain rates. Typically, convective organization measurements (SCAI, I_{org} , COP) are directly applied to satellite measurements (e.g., Tobin *et al.*, 2012; Stein *et al.*, 2017; Senf *et al.* 2018). In recent studies the indices are also used for radar data (Moseley *et al.*, 2019; Pscheidt *et al.*, 2019) or even satellite-derived rainfall (Holloway, 2017). Because the rain rate-based WOI is not yet tested for other variables such as outgoing long-wave radiation or brightness temperature, and has performed well for midlatitude rain rates, we analyze the structure of rain rates over the tropical Atlantic to characterize convective organization in this study. We refine WOI and exploit the wavelet's inherent power of localization in order to answer the following questions:

- How is convection organized over northeastern South America, tropical Atlantic and West Africa?
- Does ICON simulate convective organization correctly?
- How do environmental variables influence convective organization?

In order to explicitly quantify the role of AEWs with regard to these questions, we furthermore complement our spatial wavelet analysis with a spatiotemporal wavelet transform following Kikuchi and Wang (2010).

This article is structured as follows. Section 2 gives an overview of the ICON simulations and the observations. In Section 3 we present the WOI modifications including the extension to the local WOI (LWOI) and briefly introduce spatiotemporal wavelet transforms. After analyzing convective organization using the LWOI components, we turn to the temporal evolution of convection and link environmental quantities to the LWOI components in Section 4. We conclude the article with a summary in Section 5.

2 | MODEL AND DATA

Simulations for August 2016 are performed with a limited-area high-resolution version of the ICON model (Zängl *et al.*, 2015) within the High Definition Clouds and Precipitation for Advancing Climate Prediction (HD(CP)²) project, funded by the German Ministry for Education and Research. For detailed information on ICON we refer to Wan *et al.* (2013), Dipankar *et al.* (2015), Reinert *et al.* (2016), and Heinze *et al.* (2017).

In this study, we use ICON simulations over the tropical Atlantic with a horizontal grid spacing of $\Delta_x \approx 2.5$ km and 75 terrain following full levels (76 half levels) up to a height of about 30 km. Simulations over 36 hr were initialized with analyses from the European Centre for Medium-Range Weather Forecasts (ECMWF) at 0000 UTC and were performed for each day in August 2016. Boundary data were provided by ECMWF every 3 hr. Because spin-up takes at least 6 hr (Heinze *et al.*, 2017), we neglected the first 12 hr and chose the last 24 hr of each simulation to fully cover August 2016. This guarantees that the model physics can evolve and, although the simulations are not continuous, they are close to the observations.

The simulations include lots of interesting features such as shallow cumulus clouds, hurricanes, squall-lines and vortex streets during August 2016 and cover the tropical Atlantic as well as parts of the South American and African continents (Klocke *et al.*, 2017). Due to the high resolution, the long simulation period and persistent convective activity over the domain, the simulations are a good basis to investigate convective organization in the Tropics. However, ICON overestimates shallow cumulus and low-level clouds, which produce weak small-scale drizzle and an increased number of small-scale features (Senf *et al.*, 2018).

The ICON output is interpolated from the original triangular model grid on to a coarser regular grid with a longitudinal extent from 67.45°W to 14.45°E and 9.55°S to

19.45°N by steps of 0.10° in both directions. This corresponds to a horizontal grid spacing of about 10 km, which is close to the effective resolution of the used ICON ($7\Delta_x - 8\Delta_x$; Heinze *et al.*, 2017). The temporal resolution of the 2D output variables is 30 min, and 3D output is available every hour.

In contrast to the object-based study with satellite data by Senf *et al.* (2018), we characterize convective organization on the basis of simulated rain rates. To compare convective organization in ICON with observations, high-resolution rain rate measurements in space and time are required. In the absence of a sufficiently dense rain-gauge network or radar observations, we rely on satellite-derived rain estimations from the Integrated Multi-satellite Retrievals for Global precipitation measurement (IMERG; Huffman *et al.*, 2015) project¹ to assess the observed state of convective organization. Our primary data sources are passive microwave (MW) radiometers from low earth orbit satellites, which constitute the most direct measurements of precipitation available. Over water bodies, emissions from falling hydrometeors near the surface can easily be separated from surface emissions due to the difference in temperature. Over land, MW measurements are mainly determined by scattering from frozen-phase hydrometeors. Both kinds of data are intercalibrated using the global precipitation measurement core satellite's active MW radiometer – essentially a space-borne radar. Over land, the data undergo further calibration to rain-gauge-derived climatologies to create the final IMERG product.

While this procedure yields the overall most trustworthy available information, it may suffer from spatial and temporal inconsistencies. The satellites used to obtain the rain fields change perpetually and the measurement principle differs over land and sea. In addition, the temporal resolution is limited to the frequency of over-passing satellites. The Goddard profiling algorithm employed in IMERG therefore uses sophisticated time interpolation and auxiliary data from infrared (IR) images to create the half-hourly dataset we use. How strongly these processing steps alter the spatial structure of the resulting rain fields remains to be seen. In order to address this uncertainty in the observations, we therefore include the IR-derived rain rates as a secondary source of information. These images are based on a single instrument on a geostationary satellite, which always covers the complete domain and delivers half-hourly data. These data are less trustworthy since precipitation is inferred indirectly from cloud-top temperatures. For example, low warm precipitating clouds

may not be detected by the IR measurement, while high cirrus clouds can potentially be mis-interpreted as rain.

We aim at a more complete comparison using two observation datasets both to one another and to the simulations. Aside from model validation, the intercomparison of different satellite observations with respect to their spectral characteristics holds some interest in itself.

3 | METHODS

3.1 | Discrete wavelet transforms

To describe spatial structures in the precipitation fields, we decompose the rain rates with a redundant discrete wavelet transform. For a comprehensive overview of wavelets and their mathematical background, we refer to Daubechies (1992).

We compute the estimated locally stationary wavelet spectrum following Eckley *et al.* (2010) with help of the R Statistical Programming Language package LS2W (Eckley and Nason, 2011). The decomposition of a $2^J \times 2^J$ field leads to a set of $2^J \times 2^J \times J \times D$ wavelet coefficients with J scales ($1, \dots, J$) and $D = 3$ directions (east–west, north–south, diagonal). Here, the j th scale corresponds to features with a spatial extent of approximately 2^j grid-points. Since the wavelet coefficients are not independent, the spectral energy is biased towards large scales where most of the information in the local spectra is redundant. The correction of this bias following Eckley and Nason (2011) may lead to negative energy values at some locations. We discuss the ramifications of this phenomenon in Section 3.3.

The wavelet analysis requires a quadratic domain with $2^n \times 2^n$, $n \in \mathbb{N}$, grid points and periodic boundaries. Thus, we pad our original output field (820×291) with zeros to obtain a field of size 1024×1024 . To reduce the gradients between the original precipitation field and the synthetic zero-precipitation regions, we follow Weniger *et al.* (2017) and Kapp *et al.* (2018) and smooth the outer 25 grid points with a linearly decreasing filter. Both largest scales (9–10; 2,560–5,120 km) are strongly influenced by the formulation of the boundary conditions. Scale 8 (1,280 km) is smaller than the domain size, but the support length of the D4 wavelet exceeded the domain size. Due to these technical issues, we focus on scales 1–7 (10–640 km) in the 2D wavelet analysis, although convection may be organized into AEWs, which act on even larger scales.

In contrast to Brune *et al.* (2018), who only studied the spatially averaged wavelet spectra, we now intend to analyze the local spectra at every grid point. The location at which we store the respective wavelet coefficient therefore

¹<https://pmm.nasa.gov/category/keywords/imerg>; accessed 1 February 2020

becomes relevant. Since the Daubechies basis functions used by Eckley *et al.* (2010) can exhibit complicated structures within a large support area, it is not entirely obvious to which grid point should be attributed an individual projection. As an *ad hoc* solution, we store each coefficient at the corresponding centre of mass of the wavelet. This guarantees that spectral energy corresponding to any individual precipitation feature is located close to the feature itself, and leads to local spectra which are relatively straightforward to interpret.

3.2 | Wavelet-based organization index (WOI)

The wavelet-based organization index (WOI) was introduced by Brune *et al.* (2018) to differentiate between organized convective structures (e.g., squall-lines, supercells, clustered multicells, MCSs) and unorganized convection (e.g., pulse storms, scattered convection). The WOI consists of three components describing the horizontal scale of precipitation (WOI_1), its intensity (WOI_2) and anisotropy (WOI_3). They are defined as

$$WOI_1 = \frac{\overline{E}_1}{\overline{E}_s + \overline{E}_1}, \quad (1)$$

$$WOI_2 = \frac{\overline{E}_s + \overline{E}_1}{r}, \quad (2)$$

$$WOI_3 = \frac{1}{3} \sqrt{\sum_d \left(\left(\frac{E_s^d - \overline{E}_s}{\overline{E}_s} \right)^2 + \left(\frac{E_1^d - \overline{E}_1}{\overline{E}_1} \right)^2 \right)}. \quad (3)$$

\overline{E}_s represents the small-scale energy on scales 1–3 (10–40 km), while \overline{E}_1 represents the large-scale energy on scales 4–7 (80–1,280 km) in the wavelet spectrum, averaged over the domain and each direction. r is the number of grid points with rain rates above zero. E_s^d stands for the small-scale and E_1^d for the large-scale domain-averaged energy in the east–west ($d = 1$), north–south ($d = 2$) and diagonal ($d = 3$) directions.

3.3 | Modified wavelet-based organization index

Negative energy induced by the bias correction of the spectral coefficients may result in a $WOI_1 > 1$ and a noisy

WOI_3 . Previous studies (Weniger *et al.*, 2017; Brune *et al.*, 2018; Kapp *et al.*, 2018) used the sharp Haar wavelet (Haar, 1910), which is also known as the first member of the Daubechies family (D1; Daubechies, 1992). Preliminary investigations have shown that negative energy is reduced drastically for higher orders of Daubechies wavelets. However, the support length of Daubechies wavelets increases with their order, resulting in less sharp localization. As a compromise between good localization and less negative energy, we choose the extremal phase D4 wavelet for all the following calculations. Remaining negative energy is set to 0 before calculating the indices.

In order to render all three components comparable, we scale WOI_3 with the factor of maximal anisotropy ($3/2\sqrt{3}$). Strong convective precipitation results in high mean spectral energy \overline{E} and is concentrated on a small number of grid points r of the total domain $N_x \cdot N_y$. To ensure that intense rain rates lead to a $WOI_2 \rightarrow 1$, we multiply the total energy by -1 and subtract the exponential term from 1. Thus, for less intense rain over larger parts of the domain, WOI_2 is 0, because

$$\exp\left(-\frac{\overline{E}}{r/(N_x \cdot N_y)}\right) \rightarrow 1.$$

The resulting WOI components describe scale (sc), intensity (in) and anisotropy (ai) of convection and are defined as

$$WOI_{sc} = \frac{\overline{E}_1}{\overline{E}_s + \overline{E}_1}, \quad (4)$$

$$WOI_{in} = 1 - \exp\left(-\frac{\overline{E}}{r/(N_x \cdot N_y)}\right), \quad (5)$$

$$WOI_{ai} = \frac{1}{2\sqrt{3}} \sqrt{\sum_d \left(\left(\frac{E_s^d - \overline{E}_s}{\overline{E}_s} \right)^2 + \left(\frac{E_1^d - \overline{E}_1}{\overline{E}_1} \right)^2 \right)}. \quad (6)$$

3.4 | Local wavelet-based organization index

For the localized analysis of convective organization, we calculate WOI_{sc} , WOI_{in} and WOI_{ai} at each rainy grid point (i, j) using

$$LWOI_{sc}(i, j) = \frac{E_1(i, j)}{E_s(i, j) + E_1(i, j)}, \quad (7)$$

$$LWOI_{in}(i, j) = 1 - \exp(-E(i, j)), \quad (8)$$

$$\begin{aligned} & \text{LWOI}_{\text{ai}}(i, j) \\ &= \frac{1}{2\sqrt{3}} \sqrt{\sum_d \left\{ \left[\frac{E_s^d(i, j) - E_s(i, j)}{E_s(i, j)} \right]^2 + \left[\frac{E_l^d(i, j) - E_l(i, j)}{E_l(i, j)} \right]^2 \right\}}, \end{aligned} \quad (9)$$

with

$$E(i, j) = \frac{1}{3 \cdot 7} \sum_d \sum_k E_k^d(i, j), \quad (10)$$

$$E_l(i, j) = \frac{1}{3 \cdot 4} \sum_d \sum_{4 \leq k \leq 7} E_k^d(i, j), E_l^d(i, j) = \frac{1}{4} \sum_{4 \leq k \leq 7} E_k^d(i, j), \quad (11)$$

$$E_s(i, j) = \frac{1}{3 \cdot 3} \sum_d \sum_{1 \leq k \leq 3} E_k^d(i, j), E_s^d(i, j) = \frac{1}{3} \sum_{1 \leq k \leq 3} E_k^d(i, j), \quad (12)$$

where $E_k^d(i, j)$ describes the wavelet spectrum at grid point (i, j) for scale $k = 1, 2, \dots, 7$ and direction $d = 1, 2, 3$. Note that the LWOI_{in} is not identical to the rain intensity, rather it denotes the total local variance integrated over all scales and directions. LWOI_{in} becomes large if there are sharp gradients in the precipitation field, as is the case for squall-lines.

The code to calculate WOI and LWOI is available as an R package *calcWOI* (Brune *et al.*, 2019), which computes the original WOI as defined in Brune *et al.* (2018), the modified WOI components defined in Section 3.3 and LWOI components of an arbitrary 2D array.

3.5 | Theory of spatiotemporal wavelet transforms

Apart from its effect on the spatial patterns of precipitation, convective organization manifests itself in the movement and life cycle of thunderstorms. Since tropical weather systems are known to propagate predominantly in zonal directions, in our case westward across the Atlantic, we can infer their spatiotemporal characteristics from the meridional mean as a function of longitude and time. To quantify and compare the size and speed of the various moving systems present in this kind of data, we employ a spatiotemporal wavelet transform (STWT) which was first applied to the analysis of tropical waves by Kikuchi and Wang (2010). Following these authors, we use the complex Morlet mother wavelet given by

$$\psi(x, t) = e^{i(k_0 x + \omega_0 t)} e^{-(x^2 + t^2)/2}. \quad (13)$$

This function of space (here longitude) x and time t is a plane wave with frequency $\omega_0 = 6$ and wave number $k_0 = \pm 6$, localized by a Gaussian envelope. Here, the sign of k_0 determines the direction of propagation. The daughter wavelets of the STWT are given by

$$\psi_{a,c,\tau,b} = \frac{1}{a} \psi \left(\frac{x-b}{a \cdot \sqrt{c}}, \frac{t-\tau}{a/\sqrt{c}} \right), \quad (14)$$

where τ denotes shift in time and b shift in space; $a > 0$ is a common scaling parameter for both directions, and the parameter $c > 0$ corresponds to the phase speed of the daughter wavelet. The power P related to one of these basis functions is given by

$$P(a, c, \tau, b) = \frac{1}{a^3 c} \left| \int_{\mathbb{R}} \int_{\mathbb{R}} f(x, t) \psi_{a,c,\tau,b}^*(x, t) dx dt \right|^2, \quad (15)$$

where the normalization $1/(a^3 c)$ guarantees that the total power integrated over all daughters equals the variance of the original data (up to a further normalization dependent only on the choice of mother wavelet). Before applying the transform given by Equation (15) to the meridional means, we add zeros around the data to get a square field of $2^{11} \times 2^{11}$, thereby avoiding aliasing while speeding up the fast Fourier transformation used to perform the convolutions.

Kikuchi and Wang (2010) demonstrate how the parameters a and c can be related to the frequency ω and wavenumber k of the corresponding Fourier transform. While c is exactly the usual phase speed ω/k , the interpretation of a , which scales time and space alike, is less straightforward. To facilitate the interpretation of our results, we therefore replace a by the wavelength

$$\lambda = \frac{2\pi}{k} = 4\pi a \frac{\sqrt{c}}{\left(k_0 + \sqrt{k_0^2 + 2}\right)}.$$

For a derivation of this identity, as well as further technical details, the reader is referred to Kikuchi and Wang (2010) and references therein. Lastly, a natural way to represent the direction of the daughter wavelets, originally determined by k_0 , is to attach the sign of k_0 to the phase speed, meaning that the daughter denoted by $c = -10$ corresponds to $k_0 = -6, c = 10$.

In principle, we could apply the same discrete two-dimensional wavelet transform to the longitude–time diagrams. For two reasons, we use the STWT basis described above. Firstly, we expect the meridional means to exhibit inherently wave-like behaviour (Figure 4). The complex Morlet wavelet, which is simply a localized plane wave, therefore seems appropriate. Secondly, the spatial

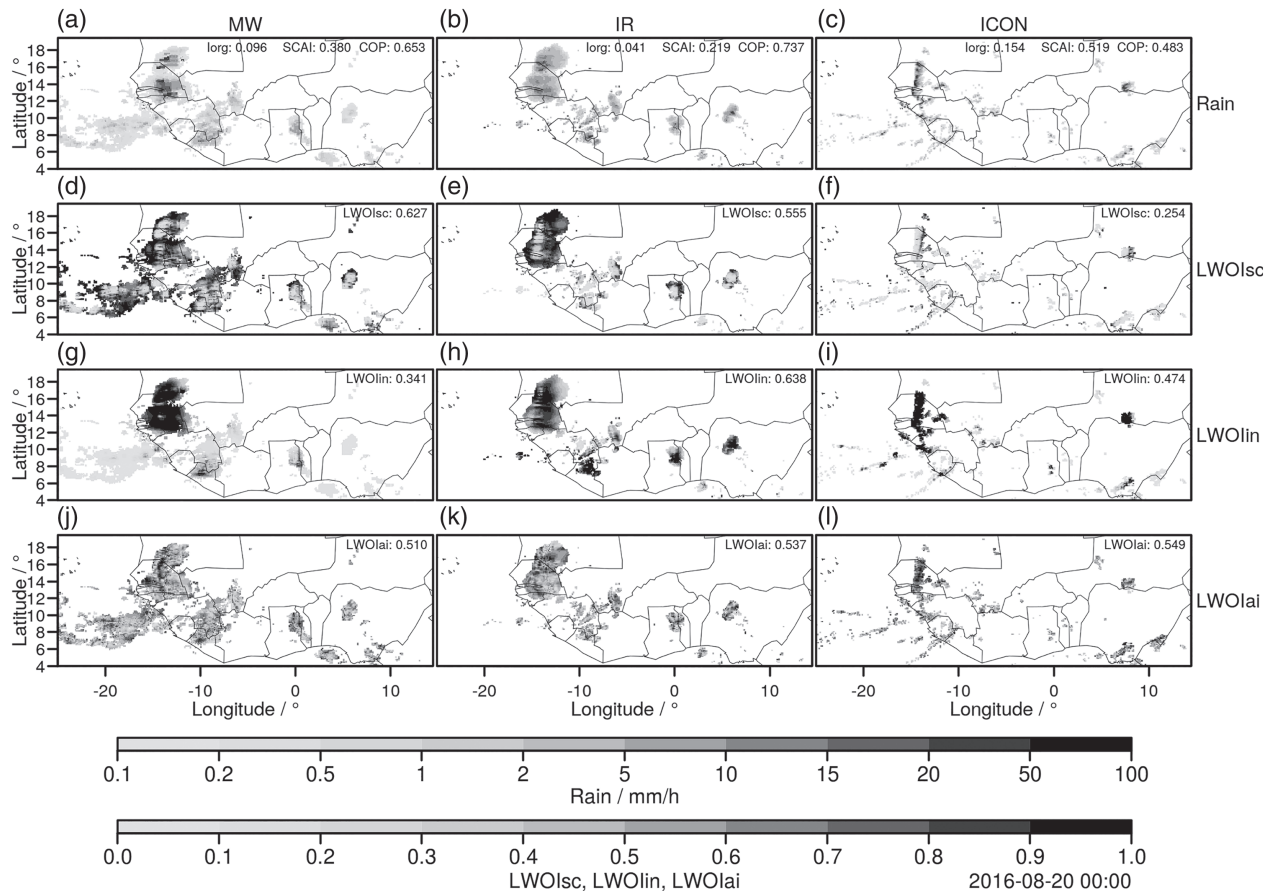


FIGURE 1 Snapshot of (a–c) rain rate in mm hr^{-1} , (d–f) LWOI_{sc} , (g–i) LWOI_{in} and (j–l) LWOI_{ai} of a West African squall-line at 0000 UTC on 20 August 2016 represented in (a, d, g, j) microwave observations, (b, e, h, k) infrared observations, and (c, f, i, l) ICON simulations. Only grid points with rain rates $\geq 0.1 \text{ mm}\cdot\text{hr}^{-1}$ are displayed. In (a–c) the organization index (I_{org} ; Tompkins and Semie, 2017), the simple convective aggregation index (SCAI; Tobin *et al.* 2012) and the convective organization potential (COP; White *et al.* 2018) are shown for the same threshold ($0.1 \text{ mm}\cdot\text{hr}^{-1}$). In (d–l), the spatial average of LWOI_{sc} , LWOI_{in} and LWOI_{ai} are shown at top right

transform is limited to three directions, allows only scales which are powers of 2, and neglects the important larger scales. For spatiotemporal data, the basis functions correspond to exactly three distinct phase speeds, combined with periods of half a month, a quarter of a month and so on. The continuous STWT entails basis functions which are directly related to any desired combination of speed and scale, making it far more convenient for this purpose.

4 | RESULTS

4.1 | Convective organization of an African squall-line

To illustrate the different representations of convective organization in MW observations, IR observations, and ICON simulations, we show rain rates and the LWOI components on 20 August 2016 at 0000 UTC in Figure 1. A westward-moving squall-line developed during 19 August

2016 and travelled to West Africa. The position of the squall-line is similar in both observations and ICON, but the intensity and its east–west extent differ. In the observations there are two local precipitation maxima in the squall-line, while ICON simulates a more uniform, meridionally oriented precipitation line. The horizontal extent of the squall-lines is largest in the MW observations and slightly smaller in the IR observations. ICON simulates much finer structures and a narrow squall-line. In addition to the heavy precipitation event in West Africa, the MW observations include lots of weak and large-scale precipitation over the Eastern Atlantic, which is almost completely missing in the IR observations. ICON simulates more maritime rainfall than IR, but the precipitation features are smaller and more intense than in MW observations. ICON fails to simulate correctly the location of the single-cell storms over the African continent, but their structure and intensity is represented more satisfactorily.

LWOI_{sc} indicates that most precipitation features in the MW observations act on large scales. In IR only

the squall-line is characterized as a large-scale feature ($LWOI_{sc} > 0.9$), while other continental cells are of small scale ($LWOI_{sc} < 0.2$). In the ICON simulation $LWOI_{sc}$ is larger than 0.5 only for some pixels within the squall-line and over Central Africa, while otherwise rainfall in ICON acts mostly on small scales. Both observations and ICON agree that the squall-line is intense ($LWOI_{in} \approx 1$). The continental cells are less intense in MW than in IR or ICON. Although $LWOI_{ai}$ is generally noisy, anisotropy along the squall-line seems slightly increased. Especially in ICON, the north–south oriented squall-line is characterized as a linearly organized structure with $LWOI_{ai} > 0.9$.

In Figure 1a–c we provide values of I_{org} , SCAI and COP based on rain rates $\geq 0.1 \text{ mm}\cdot\text{hr}^{-1}$ for MW, IR and ICON. Note that all three indices are not tuned for rain rates and were originally based on vertical wind velocity (I_{org}), brightness temperatures (SCAI) and outgoing long-wave radiation (COP). I_{org} suggests that organization is higher in ICON than in MW and IR, while both COP and SCAI (lower value for SCAI means higher degree of organization) indicate that MW and IR rainfall is more organized than in the ICON simulations. The spatial average of $LWOI_{sc}$ is consistent with SCAI and COP and suggests that the scale of precipitation structures in ICON is much smaller than in both observations, which results in a high number of small objects. Note that SCAI and COP are sensitive to the number of cells and the area (Pscheidt *et al.*, 2019). The reason why I_{org} characterizes ICON rain rates as most organized is because the small-scale objects are close together. Intensity ($LWOI_{in}$) and anisotropy ($LWOI_{ai}$) are not assessed by I_{org} , SCAI or COP. The LWOI components provide additional information on the spatial structure of convection. None of the other convective organization indices provide localized maps of convective organization.

4.2 | Convective organization during August 2016

Figure 2a–c display the averaged rain rates in August 2016 observed by the MW observations, the IR observations and simulated by ICON. All three datasets show intense rainfall along the ITCZ, over northern parts of South America and over West Africa. ICON underestimates precipitation along the ITCZ compared to observations and fails to reproduce strong precipitation over the mountains of northern South America and West Africa. IR and ICON precipitation show finer structures than the MW observations. The analysis of snapshots (Figure 1) demonstrates that precipitation derived from MW observations includes frequent large-scale stratiform precipitation over the Atlantic, which is completely missing in IR and underestimated in ICON. These huge discrepancies between

both observations are based on the different measuring methods. Note that the IR and MW rain rates are estimated from satellite images and may include large uncertainties because of the issues discussed in Section 3.

We calculate temporal averages of $LWOI_{sc}$, $LWOI_{in}$ and $LWOI_{ai}$ at each location to provide an averaged characterization of local convective organization as displayed in Figure 2d–l. For this climatology we use the same mask for both observations and ICON. Only grid points with rain rates $\geq 0.1 \text{ mm}\cdot\text{hr}^{-1}$ for at least 2% of all 31×48 timesteps in MW, IR and ICON were taken into account to focus on the main precipitation regions and to exclude the incorrectly simulated drizzle in ICON. ICON reveals much smaller scales ($LWOI_{sc}$ in Figure 2d–f) compared to both observations due to the missing large-scale stratiform precipitation. In MW observations, the stratiform rainfall over the tropical Atlantic seems much larger in scale. In ICON and IR observations, African convection acts on the largest scales. This mismatch may be caused by the different satellite measurement method over ocean and land. However, ICON and both observations suggest that convection over the western tropical Atlantic and South America is of smaller scale than over Africa and eastern parts of the tropical Atlantic. Convection over South America is very localized. The large-scale features over Africa are associated with westward-propagating MCSs.

ICON and IR observations agree on the existence of intense West African rainfall caused by MCSs, but show differences over the ocean and South America, where ICON simulates weaker precipitation (Figure 2g–i). There are five local $LWOI_{in}$ maxima in MW observations, namely over the Guiana Shield, central tropical Atlantic, West African coast along the Guinea Highlands, Ghana and Gulf of Guinea west of Mount Cameroon. Especially over the eastern half of the tropical Atlantic, the $LWOI_{in}$ is low, although MW-derived precipitation is high (Figure 2a). Thus, in the MW observations rainfall from the large-scaled systems is less intense and more persistent. In contrast, rainfall estimated from IR satellite images is very intense over the tropical Atlantic (high $LWOI_{in}$), but smaller in scale as seen before. These contrary results are due to the different measurement methods discussed in Section 2.

Anisotropy (Figure 2j–k) is slightly lower over South America and parts of West Africa in the MW observations than in ICON simulations and IR observations, but generally the ICON simulations and observations agree well in this respect. The variability of the $LWOI_{ai}$ over the complete domain is relatively small, mainly due to two reasons. Firstly, due to a missing rotational invariance of the two-dimensional wavelets used here, the $LWOI_{ai}$ is not completely invariant with respect to rotation, that is $LWOI_{ai}$ changes when a squall-lines changes

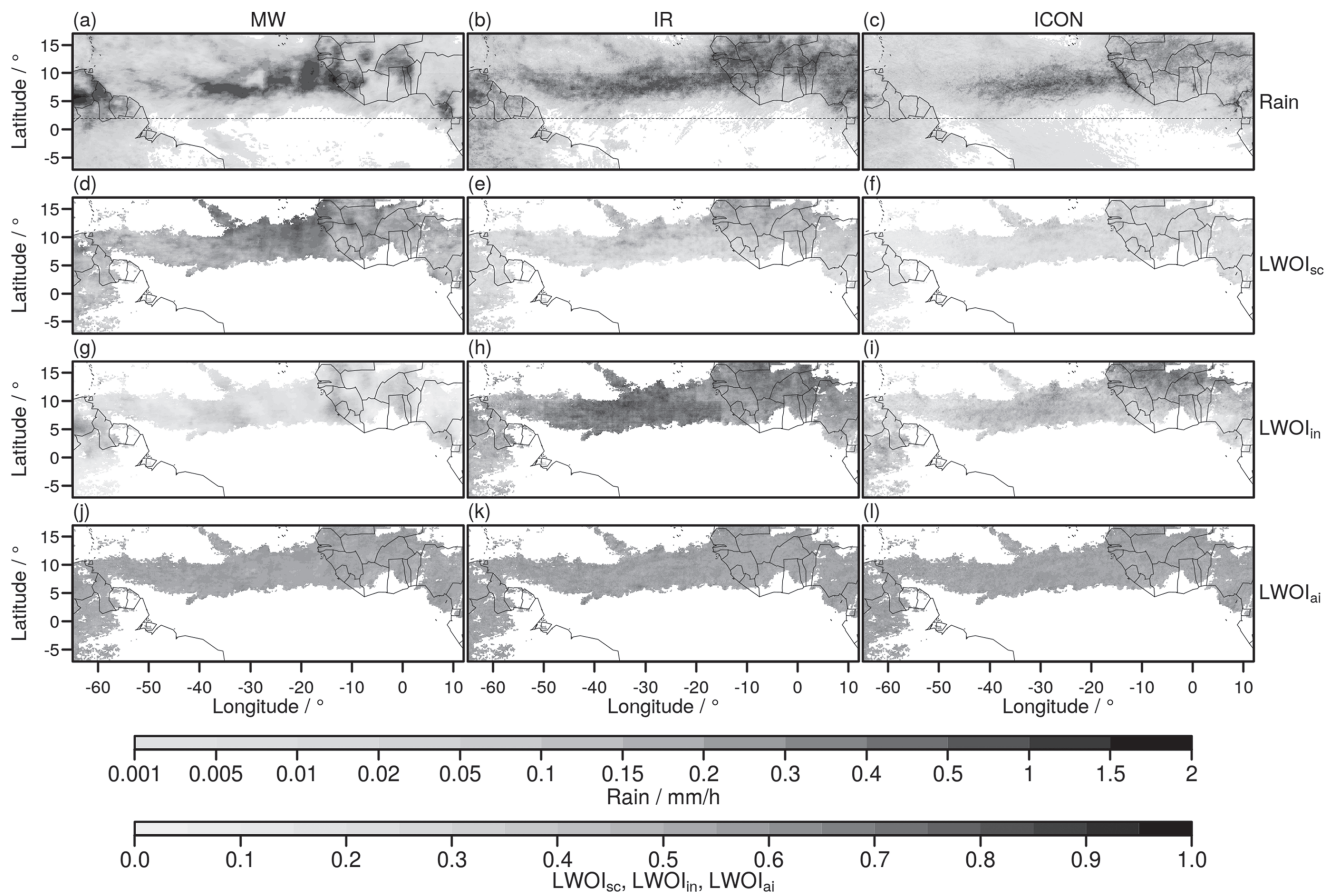


FIGURE 2 Monthly averaged (a–c) rain rates, (d–f) scale $LWOI_{sc}$, (g–i) intensity $LWOI_{in}$ and (j–l) anisotropy $LWOI_{ai}$ of precipitation during August 2016 in (a, d, g, j) MW, (b, e, h, k) IR and (c, f, i, l) ICON. $LWOI_{sc}$, $LWOI_{in}$ and $LWOI_{ai}$ are only shown for grid points with rain rates $\geq 0.1 \text{ mm}\cdot\text{hr}^{-1}$ for at least 2% of all timesteps in both observations and ICON. Dashed lines in (a–c) indicate latitude 2°N

its orientation. This may be relevant since meridionally oriented squall-lines over northern West Africa often propagate southwestwards at the end of their life cycle and change their orientation from north–south to diagonal. Secondly, convection over the tropical Atlantic may also organize into highly isotropic structures such as hurricanes. Thus although $LWOI_{in}$ is large, this results in a low $LWOI_{ai}$. $LWOI_{ai}$ as a single indicator thus may miss highly organized structures, but can be useful to differentiate a squall-line from a highly organized isotropic cluster, which both have a large $LWOI_{in}$. Because of the rotation issue and the noise in $LWOI_{ai}$, we concentrate on $LWOI_{sc}$ and $LWOI_{in}$ in the remainder of the article.

Nevertheless, to investigate the preferred orientation of precipitation patterns, we compare the scale-averaged spectral energy for each direction and show the percentage of east–west and north–south oriented objects during August 2016 in Figure 3. The orientation of each rain pixel is given as the direction of maximal energy. East–west (Figure 3a–c), north–south (Figure 3d–f) and diagonal (not shown) sum up to 1. East–west and north–south oriented objects are dominating. Only less than 10% of the objects

have a diagonal orientation, which is mainly due to the missing rotational invariance of the wavelet transform. Observations and ICON both show that convection is more zonally (east–west) oriented over the tropical Atlantic along and south of the ITCZ, while continental convection over Africa is mostly organized into meridionally (north–south) oriented squall-lines. Interestingly, MW, IR and ICON indicate that convection is also north–south oriented north of the ITCZ over the tropical Atlantic. This signal in orientation may be caused by eastward-moving squall-lines. Convection over South America shows no preferred direction.

4.3 | Temporal evolution of convection

Figure 4a–c present Hovmöller diagrams of the observed and simulated rain rates. Because most convective activity is concentrated over the northern half of the domain (Figure 2), we average the rain rates between 2°N and 17°N . ICON reproduces the large-scaled rainfall over the tropical Atlantic and daily convection over West

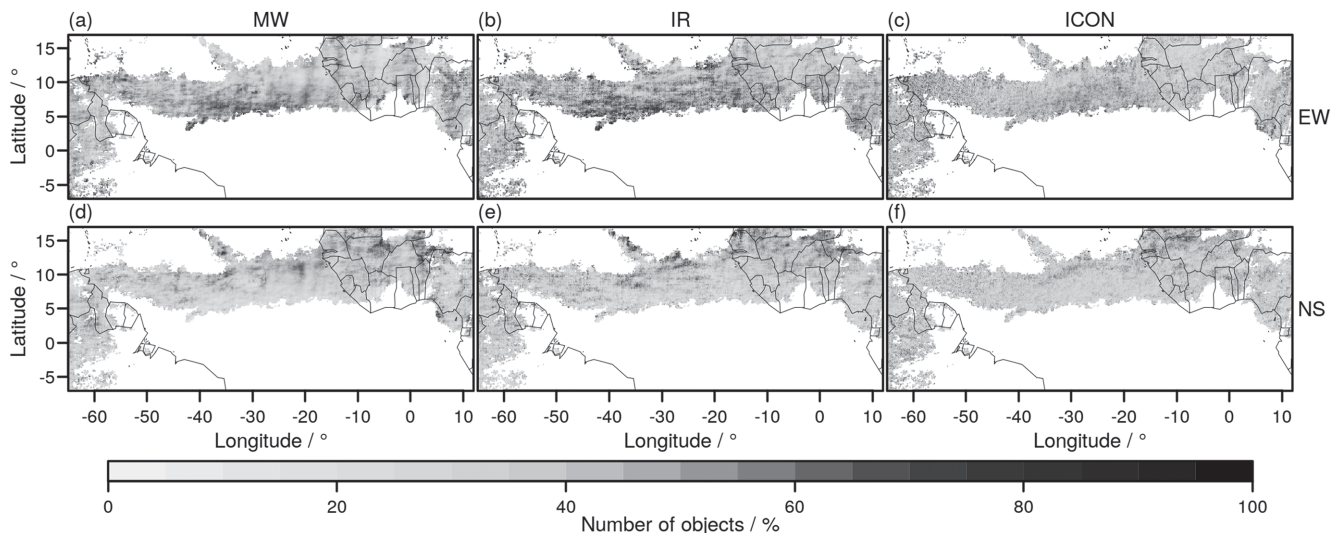


FIGURE 3 Preferred orientation of rain rate objects. Percentage of (a–c) east–west (EW) and (d–f) north–south (NS) oriented objects in (a, d) MW, (b, e) IR and (c, f) ICON

Africa very well. Only over South America and the Caribbean does ICON underestimate convective precipitation slightly. The close agreement between observations and simulations is mainly due to the initialization which takes place each 24 hr. During August 2016, approximately eight heavy precipitating clusters move from Africa to the west. All of them are clearly visible in the 700 hPa vorticity shown in Figure 4d. Especially the vorticity anomalies between 14 and 23 August 2016 are relatively strong and initiate the tropical storm *Fiona* and hurricane *Gaston* (Category 3).

Wavelets may be used to describe convective organization not only in space but also in time. The two-dimensional discrete wavelet investigates the time-averaged degree of convective organization in space, but ignores the longevity and propagation speed of the precipitating systems. Figure 4 has shown us that the central part of the domain is traversed by a number of large, westward-moving clusters with elevated degrees of spatial organization. In the light of the analyses presented by Schlueter *et al.* (2019), we expect that these large, intense, anisotropic features should be related to AEWs. To verify this hypothesis and to quantify the spatiotemporal variability of our three datasets, we apply the STWT as described in Section 3.5 to the meridionally averaged rain fields. Phase speeds are varied within a range of $10 \leq |c| \leq 100 \text{ km}\cdot\text{hr}^{-1}$ and the considered wavelengths range from 150 to 4,000 km.

Figure 5 shows the resulting wavelet spectra averaged over space and time. As expected, almost all spectral power is concentrated on the westward-moving side ($c < 0$). The largest values correspond to daily and sub-daily time-scales (i.e., small wavelengths and slow to moderate

speeds). IR has the overall greatest variability in this regime, while spectral energy in ICON is concentrated on the smallest scales ($\lambda < 250 \text{ km}$, $k > 20$). The two satellite datasets feature a notable increase in power at $T = 1$ day, which is not as pronounced in ICON. This decreased prominence of a diurnal cycle in the model is likely related to the overall weak simulated precipitation over South America which varies mostly on daily time-scales (cf. Figure 4).

As mentioned in Section 1, AEWs are characterized by periods of 2.5 to 5 days and zonal wavenumbers of 8 to 19, which roughly corresponds to wave numbers 1 to 5 in our domain. We recognize that all three datasets contain a distinct increase in power for $2.5 < T < 5$ days, with a common local maximum at the small-scale edge of the AEW regime ($c \approx -25 \text{ km}\cdot\text{hr}^{-1}$, $\lambda \approx 1,900 \text{ km}$).

Our wavelet approach makes it very straightforward to localize this AEW pattern in space and time. Instead of averaging over these two dimensions, we simply average the full spectra over all speeds and wavelengths corresponding to the features of interest (thick lines in Figure 5). In Figure 6, we have superimposed the resulting contours of AEW-related power on the original Hovmöller diagrams of rain (repeated from Figure 4). As expected, all local maxima correspond to the large, long-lived systems crossing the Atlantic with most power lying close to the African coast (20°W). Besides three dominant features persisting between 13 and 25 August 2016, we recognize one large system ending its life cycle near the beginning of the month and one beginning its westward journey near the end. While ICON has less power overall, related to generally lower intensities, the timing and locations are very similar to those of the satellite data.

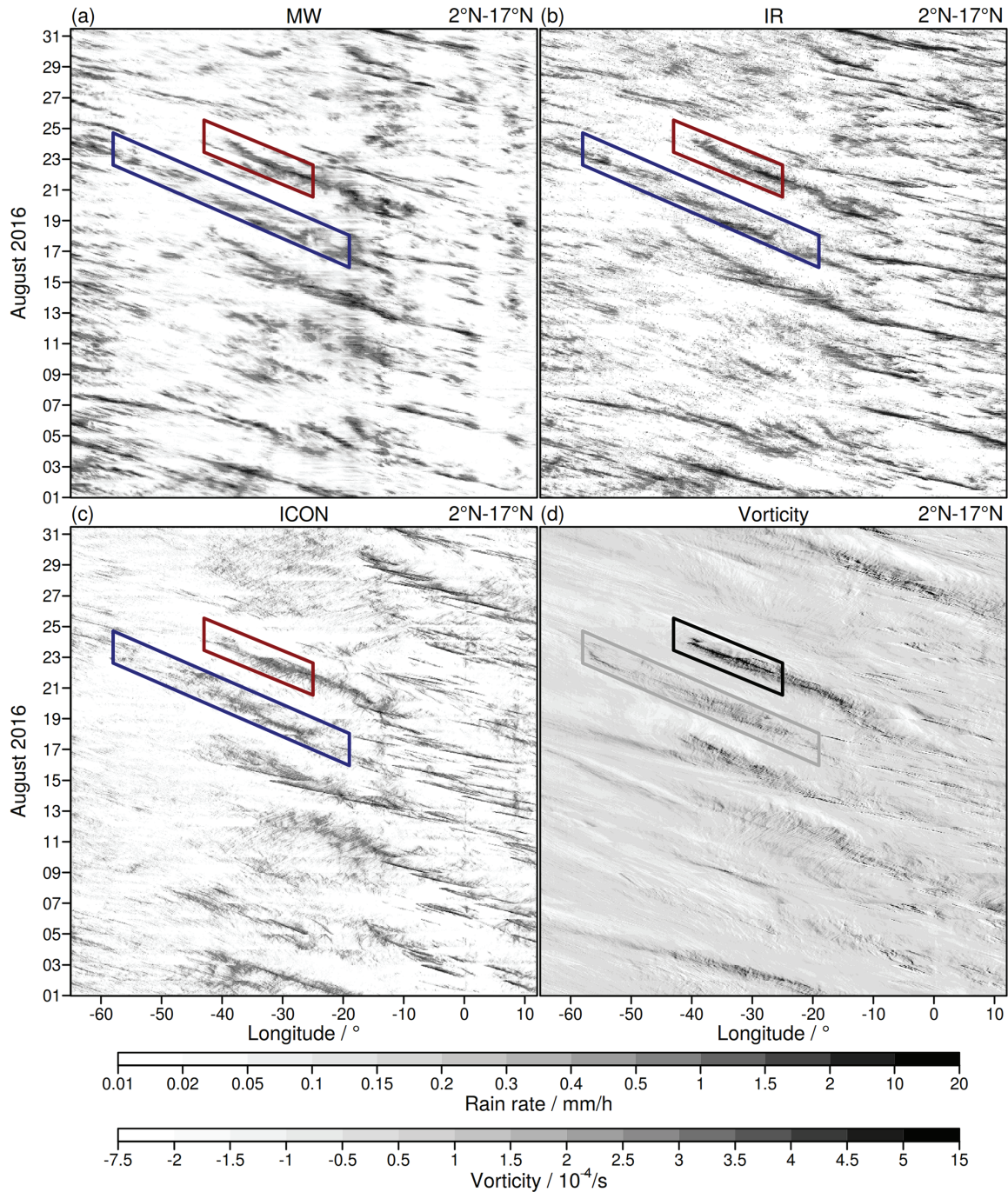


FIGURE 4 Hovmöller diagrams of (a) MW rain rate, (b) IR rain rate, (c) ICON rain rate and (d) height-averaged vorticity between model levels 51 and 53 (approximately 700 hPa). All variables are averaged between 2°N and 17°N (Figure 2). Boxes show the tropical storm *Fiona* (darkgray) and category 3 hurricane *Gaston* (black)

To enable a more direct comparison between model and observations, we summarize the time-averaged STWT spectra by calculating their barycentres in the λ - c plane, giving us one central speed and wavelength for every longitude. The resulting profiles (Figure 7) reveal the expected structure. Small, fast features dominate over the African continent and gain spatial extent while slowly losing speed over the ocean – the latter can be observed as a slight

upwards bend of the diagonal stripes in Figure 4. The characteristics over South America are similar to West Africa, albeit with a tendency towards even smaller scales. The three datasets are in fairly good agreement, particularly over the ocean where AEWs are most prevalent. Differences between model and observations are more pronounced over the continents. ICON simulates lower speeds over northwestern South America and smaller

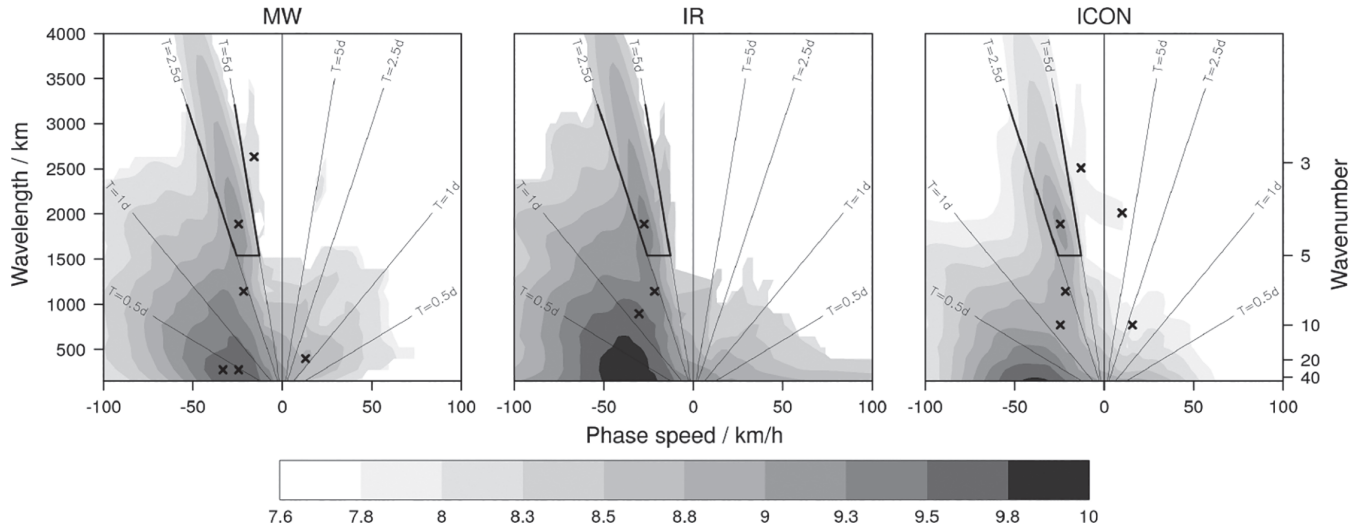


FIGURE 5 STWT spectrum (logarithmic colour levels) of the meridionally averaged rain fields as a function of phase speed and wavelength from (a) MW, (b) IR, and (c) ICON. Crosses mark all local extrema, and thick lines indicate the range of periods and wave numbers associated with AEWs. Values below the respective medians are shown in white

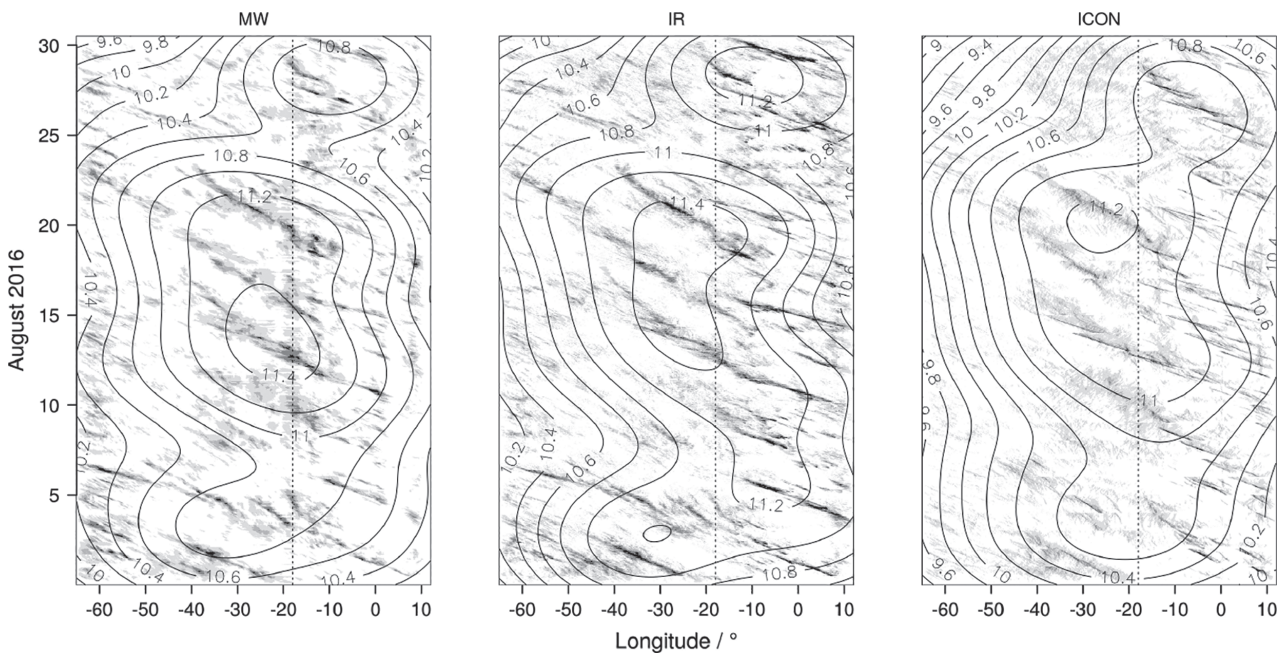


FIGURE 6 Homöller diagrams of precipitation (shading) and logarithm of power (contours) corresponding to AEWs from (a) MW, (b) IR and (c) ICON. The vertical dotted line indicates the West African coast

scales for West Africa, but the differences generally remain of the same order as the discrepancies between MW and IR.

4.4 | Link to environmental variables

The previous analysis suggests that tropical convection is organized into westward-moving squall-lines over West

Africa, while convection over the tropical Atlantic is more persistent and zonally oriented. Now we investigate convective organization over the tropical domain from a dynamical perspective using the ICON-simulated 2D and 3D variables.

To this end, we select a set of 30 environmental variables and additionally calculate hourly tendencies of nine variables such as the consumption of CAPE or changes in surface pressure within an hour before the onset of

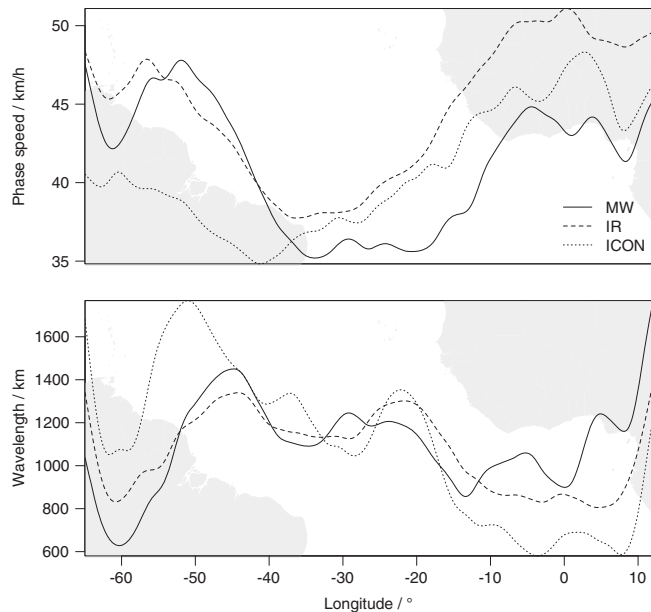


FIGURE 7 (a) Central speed and (b) wavelength as a function of longitude. A geographical map is added to the background for orientation

convection and during convection. Because most of the precipitation along the tropical Atlantic is convective, we assume convection if rain rates are above $0.1 \text{ mm}\cdot\text{hr}^{-1}$. We calculate the environmental variables for all rain pixels during August 2016. The temporal resolution of the 2D and 3D variables is 1 hr. To assess sampling uncertainty, we perform a five-day block bootstrapping. Six blocks of five running days are randomly chosen with replacement to generate 200 bootstrap samples each of $30 \times 24 = 720$ hr. We calculate meridional averages of the environmental variables and the LWOI components for each sample, and compute the temporal correlations between the environmental variables and LWOI_{sc} and LWOI_{in} as shown in Table 1. The spread of the 95% sampling interval in Table 1 and Figure 8 indicates the null hypothesis that a correlation may be due to random chance. Correlations outside these intervals are significant.

LWOI_{sc} is positively correlated with the tendency of CAPE (0.27) and the 6 km wind shear (0.24). CAPE consumption and high wind shear leads to more large-scale rain rates such as are caused by squall-lines. Surprisingly, CAPE itself is negatively correlated with LWOI_{sc} (-0.25), meaning that precipitation acts on smaller scales when CAPE is high. However, this negative correlation is reversed over the central Tropical Atlantic, as seen in Figure 8e and discussed below. Correlations between LWOI_{in} and environmental quantities are higher than for LWOI_{sc}. Strong correlations between LWOI_{in} and maximum vertical wind velocity (0.64), mean vertical wind velocity (0.60), upper-level divergence (0.58) and

column-integrated relative humidity (0.53) indicate that rain rates are particularly intense with high LWOI_{in} in the case of powerful updraughts in a humid environment.

We describe the six best correlating environmental variables (Table 1) in more detail and discuss their regional variations. Figure 8c shows that the temporal correlations between meridionally averaged LWOI_{sc} and CAPE tendency are slightly positive (0.2) for all longitudes. The scale of convection gets larger when more CAPE is consumed by convection. The temporal average of CAPE tendency shows that the large-scaled African squall-lines consume up to $500\text{--}800 \text{ J kg}^{-1} \text{ hr}^{-1}$. Over the Atlantic and along the African coast, rainfall reduces CAPE by $100 \text{ J kg}^{-1} \text{ hr}^{-1}$ or less, although LWOI_{sc} is large. CAPE is also strongly reduced over South America and the Caribbean, where temporal averages of LWOI_{sc} indicate less organized rainfall. Thus, the tendency of CAPE does not directly determine the scale of convection.

Correlations between LWOI_{sc} and CAPE (Figure 8e) are even negative over both continents (-0.25) and maximal over the central tropical Atlantic (0.35). We conclude that high CAPE over the tropical Atlantic leads to large-scale precipitation, while the degree of organization over the South American and African continents does not depend on the amount of CAPE. The monthly averages show that CAPE is high over the West Atlantic ($1,500 \text{ J kg}^{-1}$) and below $1,000 \text{ J kg}^{-1}$ over central tropical Atlantic and Africa, although LWOI_{sc} indicates large-scale precipitation. This confirms that the influence of CAPE on LWOI_{sc} is relatively small over both continents.

Wind shear over 6 km is slightly positively correlated with LWOI_{sc} (Figure 8g). High wind shear fosters the evolution of large-scale systems such as squall-lines characterized by a large LWOI_{sc}. The averaged wind shear is large over most parts of Africa ($15 \text{ m}\cdot\text{s}^{-1}$), moderate over the West and Central Atlantic ($5\text{--}10 \text{ m}\cdot\text{s}^{-1}$) and low over the East Atlantic (below $5 \text{ m}\cdot\text{s}^{-1}$) and fits well to the LWOI_{sc} pattern shown in Figure 8a. Increased CAPE values in combination with moderate wind shear north of the ITCZ may be responsible for the north–south orientated convection in this region as observed in Figure 3.

Temporal correlations between LWOI_{in} and the maximum vertical wind, upper-level divergence and column-integrated relative humidity show a similar pattern. Between 65°W and 50°W , correlations are nearly constant, increase over the tropical Atlantic and maximize at 30°W , decrease slightly towards the West African coast and remain constant over West Africa. Correlations between the environmental variables and LWOI_{in} are much larger than for LWOI_{sc} and indicate that LWOI_{in} is directly linked to the updraught velocity, especially over the Atlantic and the African continent, and the column-integrated humidity. The maximum of the

TABLE 1 Correlations over time of $LWOI_{sc}$ and $LWOI_{in}$ with the 39 environmental variables at calculation height z and time t (B denotes the value 1 hr before onset of convection, D the value at the onset of convection, and BD the difference between values at onset of convection and at 1 hr before)

Variables	Description	z (km)	t	$LWOI_{sc}$	$LWOI_{in}$
CAPE	Conv. available pot. energy	—	B	** -0.25 (-0.20,-0.16)	-0.12 (-0.11,-0.06)
dCAPE	CAPE tendency	—	BD	** 0.27 (0.08, 0.13)	** -0.29 (-0.02, 0.03)
CIN	Convective inhibition	—	B	0.03 (-0.01, 0.04)	0.16 (0.01, 0.06)
dCIN	CIN tendency	—	BD	-0.06 (-0.06,-0.04)	0.02 (-0.03, 0.00)
CLCT	Total cloud cover	—	D	0.05 (0.10, 0.14)	** 0.35 (0.04, 0.10)
dCLCT	CLCT tendency	—	BD	-0.11 (-0.09,-0.06)	-0.04 (-0.04,-0.02)
COLRH	Column-integrated rel. hum.	0.0–30.0	B	0.05 (0.06, 0.14)	** 0.53 (0.02, 0.12)
DIVSURF	Divergence	0.0– 1.7	D	0.06 (-0.04,-0.00)	0.00 (-0.02, 0.02)
DIVTOP	Divergence	8.5–15.0	D	-0.09 (-0.00, 0.04)	** 0.58 (0.01, 0.10)
PMSL	Mean sea level pressure	surface	B	0.07 (0.02, 0.08)	-0.16 (-0.03, 0.03)
dPMSL	PMSL tendency	surface	BD	-0.09 (-0.04,-0.01)	** 0.21 (0.03, 0.06)
PVMID	Potential vorticity	1.7– 8.5	D	0.05 (0.01, 0.04)	0.11 (-0.01, 0.03)
PVTOP	Potential vorticity	8.5–15.0	D	-0.06 (-0.07,-0.02)	** -0.25 (-0.06, 0.01)
RH2M	Relative humidity	0.002	B	0.05 (0.07, 0.12)	0.16 (0.03, 0.08)
dRH2M	RH2M tendency	0.002	BD	-0.16 (-0.10,-0.07)	0.03 (-0.05,-0.01)
SHEARU3	Wind shear (u)	0.8–3.0	B	-0.12 (-0.11,-0.06)	0.06 (-0.05, 0.01)
SHEARU6	Wind shear (u)	0.8–6.0	B	-0.16 (-0.16,-0.10)	0.12 (-0.07, 0.01)
SHEARV3	Wind shear (v)	0.8–3.0	B	-0.17 (-0.15,-0.09)	-0.02 (-0.08,-0.01)
SHEARV6	Wind shear (v)	0.8–6.0	B	-0.13 (-0.12,-0.07)	0.08 (-0.06, 0.01)
SHEARWS3	Wind shear speed	0.8–3.0	B	0.19 (0.09, 0.17)	** 0.20 (0.01, 0.10)
SHEARWS6	Wind shear speed	0.8–6.0	B	** 0.24 (0.16, 0.21)	0.14 (0.04, 0.10)
T2M	Temperature	0.002	B	-0.13 (-0.13,-0.10)	-0.16 (-0.09,-0.05)
dT2M	T2M tendency	0.002	BD	** 0.20 (0.07, 0.11)	-0.18 (-0.01, 0.04)
TD2M	Dewpoint temperature	0.002	B	-0.12 (-0.07,-0.02)	-0.05 (-0.06,-0.02)
dTD2M	TD2M tendency	0.002	BD	0.13 (-0.01, 0.04)	** -0.33 (-0.06, 0.00)
THETAV	Virtual potential temp.	1.7–8.5	D	0.04 (-0.04, 0.02)	0.16 (-0.01, 0.06)
U10M	U wind	0.01	B	0.14 (0.13, 0.18)	0.09 (0.03, 0.09)
dU10M	U10M tendency	0.01	BD	0.04 (-0.02, 0.00)	-0.09 (-0.02, 0.01)
U300	U wind	9.4	B	0.00 (-0.11, 0.02)	0.12 (-0.04, 0.05)
U500	U wind	5.5	B	-0.01 (0.04, 0.11)	** 0.25 (-0.00, 0.09)
V10M	V wind	0.01	B	0.10 (0.09, 0.14)	-0.06 (0.00, 0.07)
dV10M	V10M tendency	0.01	BD	-0.03 (-0.04,-0.02)	-0.02 (-0.03, 0.00)
V300	V wind	9.4	B	-0.09 (-0.06, 0.01)	-0.09 (-0.06, 0.04)
V500	V wind	5.5	B	-0.04 (-0.04, 0.02)	-0.07 (-0.05, 0.05)
WMAX	Maximum vertical wind	1.7–8.5	D	** -0.23 (-0.03, 0.02)	** 0.64 (0.00, 0.11)
WMEAN	Mean vertical wind	1.7–8.5	D	** -0.23 (-0.04, 0.00)	** 0.52 (-0.01, 0.08)
WMIN	Minimum vertical wind	1.7–8.5	D	0.03 (-0.04,-0.00)	** -0.26 (-0.07,-0.02)
WS300	Wind speed	9.4	B	0.01 (-0.02, 0.09)	-0.07 (-0.03, 0.05)
WS500	Wind speed	5.5	B	0.10 (-0.06, 0.02)	-0.11 (-0.06, 0.03)

Note: Correlations $\geq \pm 0.20$ are marked **. **Bold** font denotes the three largest correlations for $LWOI_{sc}$ and $LWOI_{in}$. 2.5 and 97.5%iles of the 200 samples are added in parentheses.

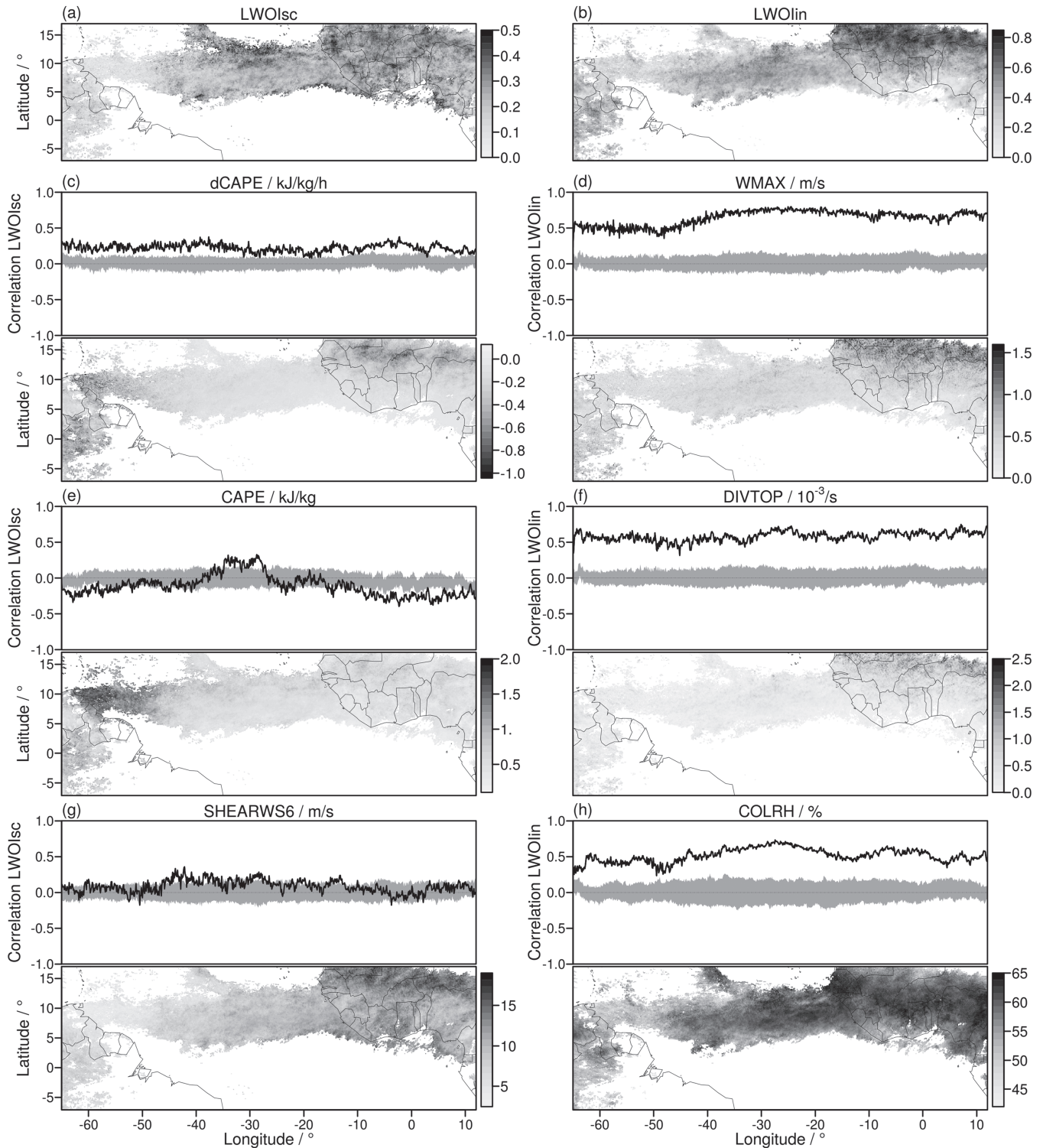


FIGURE 8 Monthly averages of (a) $LWOI_{sc}$ and (b) $LWOI_{in}$. The upper plots in (c–h) show correlations (black) and 2.5–97.5%ile ranges (grey) for (c) dCAPE and $LWOI_{sc}$, (d) WMAX and $LWOI_{in}$, (e) CAPE and $LWOI_{sc}$, (f) DIVTOP and $LWOI_{in}$, (g) SHEARWS6 and $LWOI_{sc}$, and (h) COLRH and $LWOI_{in}$. The lower plots display temporal averages of the six selected environmental variables

vertical wind velocity and the upper-level divergence in Figure 8d,f show these strong updraughts over the northern parts of West Africa, where $LWOI_{in}$ is maximal. Also over the Central Atlantic and over the South

American continent, increased updraught velocities are in accordance with an increased $LWOI_{in}$.

Our analysis demonstrates that $LWOI_{sc}$ and $LWOI_{in}$, which are calculated only on the basis of rain rates, provide

useful information on convective organization. The LWOI components detect precipitation patterns of different kinds of convective storms.

5 | CONCLUSION

Especially along the Tropics, where intense and long-lived convective systems develop, numerical weather prediction and climate models often fail to represent the degree of organization successfully. To assess the degree of convective organization and to analyze the relevant processes in detail, we use half-hourly output of high-resolution ICON simulations (grid spacing 2.5 km) over the tropical Atlantic (domain size $8,000 \times 3,000$ km) and parts of South America and West Africa during August 2016. Comparisons are made with passive microwave radiometer observations (MW) and infrared measurements (IR) from the Integrated Multi-satellite Retrievals for Global precipitation measurement project (IMERG). ICON represents convective rainfall satisfactorily; the model contains even finer structures and produces small-scale drizzle over northern and southern parts of the tropical Atlantic. The IR measurements include strong precipitation inside deep convective cores and have potentially higher spatiotemporal consistency, but miss precipitation like stratiform rain outside the updraught regions.

To identify the degree of convective organization, we modified the wavelet-based organization index (WOI). We use the Daubechies 4 instead of the Daubechies 1 (Haar) wavelet, which results in less negative spectral energy. We furthermore normalize all three WOI components between 0 (non-organized convection) and 1 (organized convection). The resulting improved WOI allows us to study convective organization on scales ranging from the complete domain to individual grid-points without any further adjustments.

There are discrepancies between convective organization simulated by ICON and observed in MW- and IR-derived rain rates. Both observations and ICON show that convection over West Africa is more organized than over South America, because the scale of convection ($LWOI_{sc}$), its intensity ($LWOI_{in}$) and anisotropy ($LWOI_{ai}$) are higher. Due to the different measurement principles, the scale of rain rates in MW observations is higher than in the IR observations and ICON. IR observations show by far the greatest intensities ($LWOI_{in} \approx 1$). $LWOI_{ai}$ indicates that convection over northern parts of West Africa is slightly more linearly organized than over South America. $LWOI_{ai}$ is not completely invariant for similar but differently oriented squall-lines, and as a single index would not identify highly organized isotropic structures over the tropical Atlantic such as hurricanes. But in combination

with $LWOI_{sc}$ and $LWOI_{in}$, the $LWOI_{ai}$ index gives useful additional information on convective clusters. However, the issue of non-invariance with respect to rotation needs to be solved to fully exploit the anisotropy information. An analysis of the predominant orientation of the wavelet spectrum shows that convection over Africa is organized into meridional squall-lines while maritime convection is preferably zonally oriented.

Studying the temporal evolution using spatiotemporal wavelet transforms (STWT), we find that in ICON the small-scale variability is higher, but the diurnal cycle of convection, especially over South America, is less pronounced. However, the large-scale AEWs ($c \approx 25 \text{ km}\cdot\text{hr}^{-1}$, $\lambda \approx 1,900 \text{ km}$, $2.5 < T < 5$ days) are simulated satisfactorily in space and time. ICON and the observations agree on the central speed and wavelength of the AEWs. They include the fast westward-moving squall-lines ($|c| > 45 \text{ km}\cdot\text{hr}^{-1}$, $\lambda < 1,000 \text{ km}$) and more persistent, slow-moving meridionally oriented convection ($|c| < 40 \text{ km}\cdot\text{hr}^{-1}$, $\lambda \approx 1,200 \text{ km}$) over the Atlantic.

We use a set of 3D variables provided by ICON to relate convective organization to convective characteristics and the environmental forcing. The pattern of scale and intensity of convection measured by $LWOI_{sc}$ and $LWOI_{in}$ correlates with different environmental variables. It turns out that $LWOI_{sc}$ is mainly modulated by wind shear. Large CAPE is not essential to simulate large-scale features, but the overlap of convective instability and strong wind shear is important. $LWOI_{in}$ is controlled by vertical wind speed and upper-level divergence, which indicate strong updraughts.

In this study, we provide a promising approach to characterize convective organization locally. Compared to the entropy analysis by Li *et al.* (2018), the LWOI components vary over the domain and are in agreement with convective and environmental quantities. The LWOI components are tested over a large domain, but only for roughly 1,500 time steps. To get a long-lasting climatology of organization over the tropical Atlantic and its temporal variability during a year, this analysis could be extended to several years. It is also possible to study convection over other regions (e.g., North America, Europe or tropical Pacific) to improve the representation of convective organization in climate and weather prediction models.

This wavelet analysis could be directly applied to IR measurements such as outgoing long-wave radiation or other variables. However, the wavelet spectra may be more sensitive for low-variation cloud structures than for small-scale highly variable rain rates.

ACKNOWLEDGMENTS

We gratefully acknowledge financial support by the project High Definition Clouds and Precipitation for Advancing

Climate Prediction HD(CP)², funded by the German Ministry for Education and Research (BMBF) under grant FKZ01LK1507B (Sebastian Brune). Special thanks go to Velibor Pejčić for his advice on the IMERG satellite data. We are also very grateful to two anonymous reviewers for their constructive comments on an earlier version of the article.

ORCID

Sebastian Brune  <https://orcid.org/0000-0002-3742-4443>

REFERENCES

- Badlan, R.L., Lane, T.P., Moncrieff, M.W. and Jakob, C. (2017) Insights into convective momentum transport and its parametrization from idealized simulations of organized convection. *Quarterly Journal of the Royal Meteorological Society*, 143, 2687–2702
- Birch, C.E., Roberts, M.J., Garcia-Carreras, L., Ackerley, D., Reeder, M.J., Lock, A.P. and Schiemann, R. (2015) Sea-breeze dynamics and convection initiation: the influence of convective parametrization in weather and climate model biases. *Journal of Climate*, 28(20), 8093–8108
- Brune, S., Kapp, F. and Friederichs, P. (2018) A wavelet-based analysis of convective organization in ICON large-eddy simulations. *Quarterly Journal of the Royal Meteorological Society*, 144, 2812–2829
- Brune, S., Buschow, S., Kapp, F. and Friederichs, P. (2019) *calcWOI: Calculates the Wavelet-based Organization Index*. <https://cran.r-project.org/web/packages/calcWOI/calcWOI.pdf>; accessed 1 February 2020. R package version 1.0.2.
- Burpee, R.W. (1972) The origin and structure of easterly waves in the lower troposphere of North Africa. *Journal of the Atmospheric Sciences*, 29(1), 77–90
- Burpee, R.W. (1974) Characteristics of North African easterly waves during the summers of 1968 and 1969. *Journal of the Atmospheric Sciences*, 31(6), 1556–1570
- Buschow, S., Pidstrigach, J. and Friederichs, P. (2019) Assessment of wavelet-based spatial verification by means of a stochastic precipitation model (wv_verif v0.1.0). *Geoscientific Model Development*, 12, 3401–3418. <https://doi.org/10.5194/gmd-12-3401-2019>
- Carlson, T.N. (1969) Some remarks on African disturbances and their progress over the tropical Atlantic. *Monthly Weather Review*, 97(10), 716–726
- Casati, B., Ross, G. and Stephenson, D. (2004) A new intensity-scale approach for the verification of spatial precipitation forecasts. *Meteorological Applications*, 11(2), 141–154
- Crétat, J., Vizy, E.K. and Cook, K.H. (2015) The relationship between African easterly waves and daily rainfall over West Africa: observations and regional climate simulations. *Climate Dynamics*, 44(1–2), 385–404
- Daubechies, I. (1992) *Ten Lectures on Wavelets*, p. 357. Society for Industrial and Applied Mathematics, Philadelphia, PA.
- Diedhiou, A., Janicot, S., Viltard, A., De Felice, P. and Laurent, H. (1999) Easterly wave regimes and associated convection over West Africa and tropical Atlantic: Results from the NCEP/NCAR and ECMWF reanalyses. *Climate Dynamics*, 15(11), 795–822
- Dipankar, A., Stevens, B., Heinze, R., Moseley, C., Zängl, G., Giorgetta, M. and Brdar, S. (2015) Large-eddy simulation using the general circulation model ICON. *Journal of Advances in Modeling Earth Systems*, 7(3), 963–986. <https://doi.org/10.1002/2015MS000431>
- Duda, J.D. and Gallus Jr., W.A. (2013) The impact of large-scale forcing on skill of simulated convective initiation and upscale evolution with convection-allowing grid spacings in the WRF. *Weather and Forecasting*, 28(4), 994–1018
- Duvel, J.P. (1990) Convection over tropical Africa and the Atlantic Ocean during northern summer. Part II: modulation by easterly waves. *Monthly Weather Review*, 118(9), 1855–1868
- Eckley, I.A. and Nason, G.P. (2011) LS2W: Implementing the locally stationary 2D wavelet process approach in R. *Journal of Statistical Software*, 43(3), 1–23. <https://doi.org/10.18637/jss.v043.i03>
- Eckley, I.A., Nason, G.P. and Treloar, R.L. (2010) Locally stationary wavelet fields with application to the modelling and analysis of image texture. *Journal of the Royal Statistical Society, Series C*, 59(4), 595–616. <https://doi.org/10.1111/j.1467-9876.2009.00721.x>
- Fink, A.H. and Reiner, A. (2003) Spatiotemporal variability of the relation between African easterly waves and West African squall lines in 1998 and 1999. *Journal of Geophysical Research: Atmospheres*, 108(D11)
- Futyan, J.M. and Del Genio, A.D. (2007) Deep convective system evolution over Africa and the tropical Atlantic. *Journal of Climate*, 20(20), 5041–5060
- Garstang, M., Massie Jr., H.L., Halverson, J., Greco, S. and Scala, J. (1994) Amazon coastal squall lines. Part I: structure and kinematics. *Monthly Weather Review*, 122(4), 608–622
- Groenemeijer, P., Púčik, T., Holzer, A.M., Antonescu, B., Riemann-Campe, K., Schultz, D.M., Kühne, T., Feuerstein, B., Brooks, H.E., Doswell III, C.A., Koppert, H.-J. and Sausen, R. (2017) Severe convective storms in Europe: ten years of research and education at the European Severe Storms Laboratory. *Bulletin of the American Meteorological Society*, 98(12), 2641–2651
- Haar, A. (1910) Zur Theorie der orthogonalen Funktionensysteme. *Mathematische Annalen*, 69(3), 331–371. <https://doi.org/10.1007/BF01456326>
- Heinze, R., Dipankar, A., Henken, C.C., Moseley, C., Sourdeval, O., Träoel, S., Xie, X., Adamidis, P., Ament, F., Baars, H., Barthlott, C., Behrendt, A., Blahak, U., Bley, S., Brdar, S., Brueck, M., Crewell, S., Deneke, H., Di Girolamo, P., Evaristo, R., Fischer, J., Frank, C., Friederichs, P., Gäocke, T., Gorges, K., Hande, L., Hanke, M., Hansen, A., Hege, H.-C., Hoose, C., Jahns, T., Kalthoff, N., Klocke, D., Kneifel, S., Knippertz, P., Kuhn, A., van Laar, T., Macke, A., Maurer, V., Mayer, B., Meyer, C.I., Muppa, S.K., Neggers, R.A.J., Orlandi, E., Pantillon, F., Pospichal, B., Räober, N., Scheck, L., Seifert, A., Seifert, P., Senf, F., Siligam, P., Simmer, C., Steinke, S., Stevens, B., Wapler, K., Weniger, M., Wulfmeyer, V., Zängl, G., Zhang, D. and Quaas, J. (2017) Large-eddy simulations over Germany using ICON: a comprehensive evaluation. *Quarterly Journal of the Royal Meteorological Society*, 143, 69–100. <https://doi.org/10.1002/qj.2947>
- Holloway, C.E. (2017) Convective aggregation in realistic convective-scale simulations. *Journal of Advances in Modeling Earth Systems*, 9(2), 1450–1472
- Holloway, C.E., Wing, A.A., Bony, S., Muller, C., Masunaga, H., L'Ecuyer, T.S., Turner, D.D. and Zuidema, P. (2017) Observing convective aggregation. *Surveys in Geophysics*, 38(6), 1199–1236
- Huffman, G.J., Bolvin, D.T. and Nelkin, E.J. (2015). Integrated Multi-satellite Retrievals for GPM (IMERG) Technical

- Documentation. https://pmm.nasa.gov/sites/default/files/document_files/IMERG_doc.pdf; accessed 1 February 2020.
- Jackson, B., Nicholson, S.E. and Klotter, D. (2009) Mesoscale convective systems over western equatorial Africa and their relationship to large-scale circulation. *Monthly Weather Review*, 137(4), 1272–1294
- Janiga, M.A. and Thorncroft, C.D. (2013) Regional differences in the kinematic and thermodynamic structure of African easterly waves. *Quarterly Journal of the Royal Meteorological Society*, 139, 1598–1614
- Janiga, M.A. and Thorncroft, C.D. (2014) Convection over tropical Africa and the East Atlantic during the West African monsoon: regional and diurnal variability. *Journal of Climate*, 27(11), 4159–4188
- Janiga, M.A. and Thorncroft, C.D. (2016) The influence of African easterly waves on convection over tropical Africa and the East Atlantic. *Monthly Weather Review*, 144(1), 171–192
- Kapp, F., Friederichs, P., Brune, S. and Weniger, M. (2018) Spatial verification of high-resolution ensemble precipitation forecasts using local wavelet spectra. *Meteorologische Zeitschrift*, 467–480
- Kikuchi, K. and Wang, B. (2010) Spatiotemporal wavelet transform and the multiscale behavior of the Madden–Julian oscillation. *Journal of Climate*, 23(14), 3814–3834
- Kiladis, G.N., Thorncroft, C.D. and Hall, N.M. (2006) Three-dimensional structure and dynamics of African easterly waves. Part I: observations. *Journal of the Atmospheric Sciences*, 63(9), 2212–2230
- Klein, C., Belušić, D. and Taylor, C.M. (2018) Wavelet scale analysis of mesoscale convective systems for detecting deep convection from infrared imagery. *Journal of Geophysical Research: Atmospheres*, 123(6), 3035–3050
- Klocke, D., Brueck, M., Hohenegger, C. and Stevens, B. (2017) Rediscovery of the doldrums in storm-resolving simulations over the tropical Atlantic. *Nature Geoscience*, 10(12), 891
- Li, Y., Yano, J.-I. and Lin, Y. (2018) Is atmospheric convection organised?: information entropy analysis. *Geophysical and Astrophysical Fluid Dynamics*, 113, 553–573. <https://doi.org/10.1080/03091929.2018.1506449>
- Liu, C., Zipser, E.J. and Nesbitt, S.W. (2007) Global distribution of tropical deep convection: different perspectives from TRMM infrared and radar data. *Journal of Climate*, 20(3), 489–503
- Lubis, S.W. and Jacobi, C. (2015) The modulating influence of convectively coupled equatorial waves (CCEWs) on the variability of tropical precipitation. *International Journal of Climatology*, 35(7), 1465–1483
- Mapes, B. and Neale, R. (2011) Parameterizing convective organization to escape the entrainment dilemma. *Journal of Advances in Modeling Earth Systems*, 3(2). <https://doi.org/10.1029/2011MS000042>
- Mathon, V. and Laurent, H. (2001) Life cycle of Sahelian mesoscale convective cloud systems. *Quarterly Journal of the Royal Meteorological Society*, 127, 377–406
- Mekonnen, A. and Rossow, W.B. (2018) The interaction between deep convection and easterly wave activity over Africa: convective transitions and mechanisms. *Monthly Weather Review*, 146(6), 1945–1961
- Mekonnen, A., Thorncroft, C.D. and Aiyer, A.R. (2006) Analysis of convection and its association with African easterly waves. *Journal of Climate*, 19(20), 5405–5421
- Möbis, B. and Stevens, B. (2012) Factors controlling the position of the intertropical convergence zone on an aquaplanet. *Journal of Advances in Modeling Earth Systems*, 4(4)
- Moncrieff, M.W. (2010) The multiscale organization of moist convection and the intersection of weather and climate. *Climate Dynamics*, 189, 3–26
- Moncrieff, M.W., Liu, C. and Bogenschutz, P. (2017) Simulation, modeling, and dynamically based parameterization of organized tropical convection for global climate models. *Journal of the Atmospheric Sciences*, 74(5), 1363–1380
- Moseley, C., Pscheidt, I., Cioni, G. and Heinze, R. (2019) Impact of resolution and air temperature on large-eddy simulation of mid-latitude summer time convection. *Atmospheric Chemistry and Physics Discussions*, 2019, 1–25. <https://doi.org/10.5194/acp-2019-638>
- Nolan, D.S., Tulich, S.N. and Blanco, J.E. (2016) ITCZ structure as determined by parameterized versus explicit convection in aquachannel and aquapatch simulations. *Journal of Advances in Modeling Earth Systems*, 8(1), 425–452
- Peters, K., Crueger, T., Jakob, C. and Möbis, B. (2017) Improved MJO-simulation in ECHAM 6.3 by coupling a stochastic multi-cloud model to the convection scheme. *Journal of Advances in Modeling Earth Systems*, 9(1), 193–219
- Petersen, W.A. and Rutledge, S.A. (2001) Regional variability in tropical convection: observations from TRMM. *Journal of Climate*, 14(17), 3566–3586
- Price, C., Yair, Y. and Asfur, M. (2007) East African lightning as a precursor of Atlantic hurricane activity. *Geophysical Research Letters*, 34(9)
- Pscheidt, I., Senf, F., Heinze, R., Deneke, H., Trömel, S. and Hohenegger, C. (2019) How organized is deep convection over Germany?. *Quarterly Journal of the Royal Meteorological Society*, 145, 2366–2384. <https://doi.org/10.1002/qj.3552>
- Reed, R.J., Norquist, D.C. and Recker, E.E. (1977) The structure and properties of African wave disturbances as observed during phase III of GATE. *Monthly Weather Review*, 105(3), 317–333
- Reinert, D., Prill, F., Frank, H. and Zängl, G. (2016). Database Reference Manual for ICON and ICON-EPS, version 1.1.9. Research and Development at DWD, Offenbach, Germany.
- Rickenbach, T.M. (2004) Nocturnal cloud systems and the diurnal variation of clouds and rainfall in southwestern Amazonia. *Monthly Weather Review*, 132(5), 1201–1219
- Rickenbach, T.M., Nieto Ferreira, R., Guy, N. and Williams, E. (2009) Radar-observed squall-line propagation and the diurnal cycle of convection in Niamey, Niger, during the 2006 African Monsoon and Multidisciplinary Analyses Intensive Observing Period. *Journal of Geophysical Research: Atmospheres*, 114(D3). <https://doi.org/10.1029/2008JD010871>
- Romatschke, U. and Houze Jr., R.A. (2010) Extreme summer convection in South America. *Journal of Climate*, 23(14), 3761–3791
- Schlueter, A., Fink, A.H., Knippertz, P. and Vogel, P. (2019) A systematic comparison of tropical waves over Northern Africa. Part I: influence on rainfall. *Journal of Climate*, 32(5), 1501–1523. <https://doi.org/10.1175/JCLI-D-18-0173.1>
- Schumacher, C. and Houze Jr., R.A. (2006) Stratiform precipitation production over sub-Saharan Africa and the tropical east Atlantic as observed by TRMM. *Quarterly Journal of the Royal Meteorological Society*, 132, 2235–2255

- Senf, F., Klocke, D. and Brueck, M. (2018) Size-resolved evaluation of simulated deep tropical convection. *Monthly Weather Review*, 146(7), 2161–2182
- Shannon, C.E. (1948) A mathematical theory of communication. *Bell System Technical Journal*, 27(3), 379–423
- Stein, T.H., Holloway, C.E., Tobin, I. and Bony, S. (2017) Observed relationships between cloud vertical structure and convective aggregation over tropical ocean. *Journal of Climate*, 30(6), 2187–2207
- Stevens, B. and Bony, S. (2013) What are climate models missing?. *Science*, 340(6136), 1053–1054
- Tobin, I., Bony, S. and Roca, R. (2012) Observational evidence for relationships between the degree of aggregation of deep convection, water vapor, surface fluxes, and radiation. *Journal of Climate*, 25(20), 6885–6904. <https://doi.org/10.1175/JCLI-D-11-00258.1>
- Tomassini, L. (2018) Mesoscale circulations and organized convection in African easterly waves. *Journal of the Atmospheric Sciences*, 75(12), 4357–4381
- Tompkins, A.M. and Semie, A.G. (2017) Organization of tropical convection in low vertical wind shears: role of updraft entrainment. *Journal of Advances in Modeling Earth Systems*, 9(2), 1046–1068. <https://doi.org/10.1002/2016MS000802>
- Wan, H., Giorgetta, M.A., Zängl, G., Restelli, M., Majewski, D., Bonaventura, L., Fröhlich, K., Reinert, D., Rípodas, P., Kornbluh, L. and Förstner, J. (2013) The ICON-1.2 hydrostatic atmospheric dynamical core on triangular grids, part I: formulation and performance of the baseline version. *Geoscientific Model Development*, 6, 735–763. <https://doi.org/10.5194/gmd-6-735-2013>
- Weniger, M., Kapp, F. and Friederichs, P. (2017) Spatial verification using wavelet transforms: a review. *Quarterly Journal of the Royal Meteorological Society*, 143, 120–136. <https://doi.org/10.1002/qj.2881>
- White, B.A., Buchanan, A.M., Birch, C.E., Stier, P. and Pearson, K.J. (2018) Quantifying the effects of horizontal grid length and parameterized convection on the degree of convective organization using a metric of the potential for convective interaction. *Journal of the Atmospheric Sciences*, 75(2), 425–450. <https://doi.org/10.1175/JAS-D-16-0307.1>
- Wing, A.A., Emanuel, K.A., Holloway, C.E. and Muller, C. (2017) Convective self-aggregation in numerical simulations: a review. *Surveys in Geophysics*, 38, 1173–1197. <https://doi.org/10.1007/s10712-017-9408-4>
- Xie, S.-P. and Carton, J.A. (2004) Tropical Atlantic variability: patterns, mechanisms, and impacts. *Earth Climate*, 147, 121–142
- Xu, W. and Zipser, E.J. (2012) Properties of deep convection in tropical continental, monsoon, and oceanic rainfall regimes. *Geophysical Research Letters*, 39(7). <https://doi.org/10.1029/2012GL051242>
- Yano, J.-I. and Jakubiak, B. (2016) Wavelet-based verification of the quantitative precipitation forecast. *Dynamics of Atmospheres and Oceans*, 74, 14–29
- Yano, J.-I., Moncrieff, M.W. and Wu, X. (2001a) Wavelet analysis of simulated tropical convective cloud systems. Part II: decomposition of convective-scale and mesoscale structure. *Journal of the Atmospheric Sciences*, 58(8), 868–876
- Yano, J.-I., Moncrieff, M.W., Wu, X. and Yamada, M. (2001b) Wavelet analysis of simulated tropical convective cloud systems. Part I: basic analysis. *Journal of the Atmospheric Sciences*, 58(8), 850–867
- Zängl, G., Reinert, D., Rípodas, P. and Baldauf, M. (2015) The ICON (ICOsahedral Non-hydrostatic) modelling framework of DWD and MPI-M: description of the non-hydrostatic dynamical core. *Quarterly Journal of the Royal Meteorological Society*, 141, 563–579. <https://doi.org/10.1002/qj.2378>
- Zipser, E.J., Cecil, D.J., Liu, C., Nesbitt, S.W. and Yorty, D.P. (2006) Where are the most intense thunderstorms on earth?. *Bulletin of the American Meteorological Society*, 87(8), 1057–1072

How to cite this article: Brune S, Buschow S, Friederichs P. Observations and high-resolution simulations of convective precipitation organization over the tropical Atlantic. *Q.J.R. Meteorol. Soc.* 2020;146:1545–1563. <https://doi.org/10.1002/qj.3751>